Annals of Biomedical Engineering, Vol. 34, No. 3, March 2006 *(© 2006)* pp. 530–544
DOI: 10.1007/s10439-005-9048-6

Numerical Solution of Ocular Fluid Dynamics in a Rabbit Eye: Parametric Effects

SATISH KUMAR,[1] SUMANTA ACHARYA,[1] ROGER BEUERMAN,[2] and ARTO PALKAMA[2]

[1]Mechanical Engineering, Louisiana State University, Baton Rouge, LA and [2]Department of Ophthalmology, LSU Eye Center, New Orleans, LA

(Received 30 January 2004; accepted 20 July 2005; published online: 1 February 2006)

Abstract—Numerical calculations of the aqueous humor dynamics in the anterior chamber of a rabbit's eye are presented to delineate the basic flow mechanisms. The calculations are based on a geometrical model of the eye, which represents the Trabecular meshwork (TM) as a multilayered porous zone of specified pore sizes and void fraction. The outer surface of the cornea is assumed to be at a fixed temperature (corresponding to the ambient temperature), while the iris surface is assumed to be at the core body temperature. Results are obtained for both the horizontal upward-facing orientation of the eye, and the vertical orientation of the eye. Parameters varied include: the temperature difference between the iris and the cornea to underscore the important role of buoyancy in driving the aqueous humor flow; and, the pupil size reflecting different levels of ambient light. Buoyancy is observed to be the dominant driving mechanism for the convective motion in both orientations of the eye. Variations in the pupil size appear to have little influence on the IOP or flow distribution in view of the dominant role of buoyancy in controlling the flow motion. The study provides distributions of the shear stress and flow patterns and delineates the important role of the eye-orientation on these results.

Keywords—Aqueous humor, Fluid dynamics, Trabecular meshwork.

INTRODUCTION

The fluid dynamics of the aqueous humor (AH) in the anterior chamber of eye and drainage mechanisms through the Trabecular Meshwork (TM) are not fully understood. The small size of anterior chamber and complexities of flow measurements inside the living eye make detailed flow data difficult to obtain. Computational simulation of the flow in the anterior chamber can therefore be very useful in producing the required understanding of the flow mechanisms. Eye diseases such as glaucoma are often linked to obstruction of the outflow and high fluid pressure inside the eye. The pressure inside the anterior chamber of the eye with respect to the atmospheric pressure is recognized as intraocular pressure (IOP). Increased IOP sustained for a long time can damage the optic nerve in the eye and can lead to blindness.[26] The goal of this paper is to perform a first-principles flow simulation using a model of a rabbit's eye and to analyze the effect of the resistance of the drainage system on the flow distribution.

Aqueous humor enters the eye in the posterior chamber, and is formed by secretion and ultrafiltration in the highly vascularized ridges projected from the ciliary body of the posterior chamber. The bulk flow rate of the aqueous humor into the anterior chamber of normal human eye varies in the range of 1.5–2.5 μl/min,[22] while for pigmented rabbits it varies in the range of 1.0–2.5 μl/min.[22] It enters the anterior chamber through the pupil between the lens and iris. More than 80% of the aqueous humor in the rabbit eye exits through the Trabecular Meshwork (TM) into the Schlemm's canal,[12] which is located in the vicinity of the junction between the iris and cornea. The aqueous humor is then discharged into the venous system, either through the aqueous veins or through the episcleral veins. Another exit pathway for the AH is the uveoscleral drainage system where the AH enters the iris root and passes between the muscle bundles in the ciliary body to the choroid and out through the episcleral tissues. This pathway contributes little to the outflow in rabbit eyes (20%) and is neglected in the present study.[12]

Blood flow in the iris and ciliary body maintain their temperature at the body temperature (37°C).[25] The outer surface of the cornea (0.6 mm thick)[29] is generally maintained at 32–33°C[17,23] by the tear film evaporation, but the inner surface of the cornea is at a higher temperature, and is only 2–4°C less than the body temperature because of the thermal resistance provided by the cornea. However, this small temperature gradient (2–4°C) across the anterior chamber is believed to be the dominant mechanism driving the fluid flow in the anterior chamber of the eye.

The outflow network system of the eye consists of a graded porous mesh from the inside of the eye to the outside. These include: (1) the uveal and corneoscleral meshwork, (2) the juxtacanalicular tissue (JCT), (3) the endothelial wall of the Schlemm's canal, (4) the Schlemm's canal, and (5) the aqueous veins. Both the uveal and corneoscleral meshwork

Address correspondence to Sumanta Acharya, Mechanical Engineering, Louisiana State University, Baton Rouge, LA 70803.

have negligible resistance because of their bigger pore size (25–75 μm).[29] It is believed that the tortuous flow passage in the JCT accounts for the most of the flow resistance[5,15] because of its very small pore size ($\sim$1.0–2.0 μm)[6,26] and the presence of the extracellular matrix gel in the open spaces.

Geometrical modeling of the TM is an extremely challenging task, and although efforts have been made to study the role of the TM and Schlemm's canal on the outflow resistance through very idealized models,[7,14,16] none of the computational flow simulations reported to date[1,10–12] have included the TM in their calculations. In the present study, the TM is modeled as an annular porous gutter with a specified pore size and void fraction.[7,18] This is the first flow simulation reported where the geometry of the TM is directly modeled.

Scott[27,28] has presented a finite element model for calculating the temperature rise in an eye induced by the exposure to infrared radiation, but the intraocular flow field was not determined in their work. Heys *et al.*[12] have developed a two-dimensional model of the coupled aqueous humor-iris system for determining the contribution of aqueous humor flow and passive iris deformation to the iris contour shape. Their model predicts the iris contour and the iris to lens contact, which is primarily a function of the aqueous flow rate, the permeability of the TM and posterior pathway and iris modulus. Heys and Barocas[10] have extended this work to predict the effects of accommodation on the iris position and the pressure distribution in the anterior chamber. The azimuthal symmetry in these models due to the neglect of the gravity and buoyancy effects, and the neglect of the effect of the TM on the pressure distribution, restricts the capabilities of the model in accurately predicting the flow mechanisms inside the eye.

The two studies reporting flow simulations in the eye, and most relevant to the present work, are those of Canning *et al.*[1] and Heys and Barocas.[11] Canning *et al.*[1] solved the flow profile inside the anterior chamber using a simplified three-dimensional computational model and analyzed the deposition of particles leading to the formation of structures inside the eye. Heys and Barocas[11] presented three-dimensional flow simulations, but neglected the effect of TM on the transport and deposition of pigment particles. Through experimental observations, the TM is believed to play a major role in the entrapment of particles through its pores.[3]

The long-term goal of the present study is to develop a model for identifying the mechanisms for the development of Krukenberg-spindles, Hyphemas and Hypopyons, which are related to the deposition of particles in the anterior chamber. The TM resistance and the strength of the buoyancy driven flow determine particle deposition rates and locations, and how they are related to different pathological conditions of the eye. The goal of the present paper is to report a comprehensive 3-dimensional flow simulation where the details of the TM are represented as a graded porous structure, and the flow patterns and the pressure distribution in the anterior chamber for different parametric conditions are analyzed to delineate key flow mechanisms and parametric effects. Both the horizontal, upward-facing orientation of the eye and the vertical orientation of the eye are considered in this paper.

MATHEMATICAL MODEL

Geometrical Model of the Rabbit's Eye

In this paper, attention is focused on a rabbit's eye, whose shape and geometry are slightly different from those of the human eye. The depth of the anterior chamber of the rabbit eye is in the range of 5–6 mm and diameter in the plane of the iris root is 12 mm. The iris, which is the front extension of the ciliary body, has a slightly elliptical shape with a vertical axis 11–12 mm long. The pupil changes its diameter depending on the amount of the light falling on the eyeball. It has been experimentally found that iris-tissue is incompressible and linearly elastic under small deformations.[12] The biconvex crystalline lens located at the back of the anterior chamber is enclosed in a capsule suspended by the ciliary body with zonular fibers. AH secreted in the posterior chamber by the ciliary body enters the anterior chamber through the small gap between the iris and lens which is estimated to be few microns ($\approx$10 μm) wide.[11] In this paper, the anterior chamber is modeled as a hemispherical geometry with a diameter of 12 mm. The iris is modeled as a rigid surface at the bottom of the hemispherical anterior chamber with a circular aperture at the center (the pupil) from which the flow enters the anterior chamber of eye. Since the velocity profile and the flow pattern in the anterior chamber is buoyancy driven it is unlikely that the inlet profile will have significant effect. Therefore, for simplicity we have assumed a flat inlet velocity profile of AH through the pupil (of radius 2.5 mm unless otherwise specified). However, the validity of this assumption is tested, as shown later.

The cornea is an avascular and transparent tissue with thermal properties close to that of water. It is modeled as a rigid hemispherical shell with a constant temperature (T_C). The temperature drop between the iris and the cornea (generally considered to be in the 2–4°C for the open eye) provides the buoyant force mechanism to drive the AH. This temperature drop is treated as a parameter in the present study, and is varied between 0.02°C (eye-lids closed) to 6°C. The AH is assumed to be viscous liquid with properties close to those of water (Table 1).

As noted earlier, the TM is treated as annular porous zone at the bottom of the anterior chamber. It is assumed to have a thickness of 1 mm normal to iris surface and an annular width of 1.2 mm in outflow direction. The part of

TABLE 1. Properties of AH used in simulations.

Properties	Value
Dynamic viscosity (μ, kg/ms)	0.001
Specific heat (C_p, J/kg-K)	4182
Density (ρ, kg/m^3)	1000.0
Thermal conductivity (K, W/m-K)	0.6
Volume expansion coefficient (β, 1/K)	0.0003

the TM immediately adjacent to the anterior chamber is the uveal meshwork followed by the corneoscleral meshwork. This part of the meshwork has negligible resistance to outflow due to its bigger pore size.[9,21] We treat this part of TM as an annular porous zone with 0.2 mm width and a resistance coefficient corresponding to 100 μm pore size and 0.5 void fraction. The remaining part of TM represents the JCT, and is treated as a porous zone (packed bed) with a specified average pore size (0.6 μm) and a void fraction of 0.5. Since the majority of the pressure drop (6 mmHg) occurs in the TM, the void fraction and width of the JCT are adjusted to achieve the desired pressure drop. Since the JCT structure is rather complex with superimposed fibrocellular sheets that are filled with extracellular matrix gel in the open spaces, the exact void fraction is difficult to determine. So in this paper, we have selected JCT parameters that will provide the right pressure drop since this is a key aspect for correct simulations. Therefore, the void fraction was arbitrarily set to be 0.5 and the width of JCT adjusted to yield the correct overall pressure drop across the TM. This width is determined to be 1000 μm, which is larger than the physiologic dimensions reported. A different void fraction of the JCT would have yielded a different width to achieve the same pressure drop, but this aspect was not considered further since the key issue was to achieve the correct pressure drop, and different combinations of void fraction and JCT would achieve the desired pressure drop.

Governing Equations

The steady three-dimensional incompressible Navier–Stokes equations are solved with the inclusion of buoyancy terms for natural convection[20,30] and Darcy pressure drop terms in the porous zone. The density appearing in the buoyancy term is assumed to satisfy the Boussinesq approximation. The resulting nondimensional forms of the momentum, energy, and continuity equations are given by Eqs. (1)–(3) below.

Momentum-equation:

$$U_j \frac{\partial U_i}{\partial X_j} = \frac{1}{Re_D}\left(\frac{\partial^2 U_i}{\partial X_j \partial X_j}\right) - \delta_{im}\left(\frac{Gr_D}{Re_D^2}\right)\theta - \frac{\partial P}{\partial X_i} \tag{1}$$

where m represents the index of the coordinate direction in which gravity is acting and δ_{im} is the Dirac-delta function. The second term in the right-hand side of Eq. (1) (buoyancy term) is included in the momentum equation only for the co–ordinate direction (denoted as m) in which the body forces are acting (gravity forces).

Energy equation:

$$U_j \frac{\partial \theta}{\partial X_j} = \frac{1}{Pr}\frac{1}{Re_D}\left(\frac{\partial^2 \theta}{\partial X_j \partial X_J}\right) \tag{2}$$

Continuity equation:

$$\frac{\partial U_j}{\partial X_j} = 0 \tag{3}$$

The following non-dimensional variables are used in Eqs. (1)–(3):

$$X = \frac{x}{D}, \quad Y = \frac{y}{D}, \quad Z = \frac{z}{D};$$
$$U = \frac{u}{U_{\text{in}}}, \quad V = \frac{v}{U_{\text{in}}}, \quad W = \frac{w}{U_{\text{in}}};$$
$$\theta = \frac{T - T_C}{T_{\text{in}} - T_C}; \qquad P = \frac{(p - \rho g x_m)}{\rho U_{\text{in}}^2}$$

where T_{in} is the temperature of AH at inlet and T_C is the corneal temperature that is used as the reference temperature for the calculation of all property values. The characteristic speed U_{in} is 2.12 μm/s and the characteristic length D is the diameter of the iris surface in the model, which is 12 mm. The important nongeometrical parameters that appear in the governing equations are the Reynolds number ($Re_D = \frac{\rho U_{\text{in}} D}{\mu}$), the Prandtl number ($Pr = \frac{C_p \mu}{k}$), and the Grashof number ($Gr_D = \frac{D^3 \rho^2 g \Delta\beta T}{\mu^2}$). Values of interest in the present study are: $Re_D = 0.025$, $Pr = 7.0$, and $Gr_D = 1.017 \times 10^2$-3.051×10^4 ($\Delta T = 0.02$–6°C). The values of Re_D and Pr chosen are representative of AH flow, while Gr_D or ΔT is parametrically varied to represent a range of corneal temperature conditions (from eye-lids closed to low ambient temperatures).

To model the flow in the porous regions representing the TM, Ergun's Eq. (4) is solved where the pressure gradient term ($\frac{\partial p}{\partial x_i}$) is represented by the sum of a viscous loss term (the Darcy term) and an inertial loss (Brinkman) term. Thus,

$$-\frac{\partial p}{\partial x_i} = \frac{\mu}{\alpha} u_i + C_2 \frac{\rho}{2} |u_i| u_i \tag{4}$$

which, in nondimensional form, is written as

$$-\frac{\partial P}{\partial X_i} = \frac{D^2 U_i}{\text{Re}_D \alpha} + \frac{C_2}{2} D |U_i| U_i \tag{5}$$

The porous media model (Eq. (5)) incorporates empirically determined flow resistances (specified through the permeability α and the inertial resistance factor C_2) in the porous region. Equation (5) combined with the continuity equation provides a solution to the velocity field in the porous zone. In laminar flows through porous media, the

pressure drop is typically proportional to velocity. An order of magnitude analysis shows that the viscous term (first term) in Eq. (4) is more important compared to the inertial resistive term (second term). The inertial term can therefore be neglected from the above equations for the porous zone; however, the term is included in the code used here, and is retained in the simulations for completeness. It should be noted that a preliminary calculation of the Brinkman's term indicates that this term is small (order of 0.001) and can be neglected.

To get appropriate values of the constants α and C_2, a semiempirical correlation, derived from the Ergun equation[4] is used. These correlations for the permeability α and inertial resistance factor C_2 are applicable over a wide range of Reynolds number and for various packing levels, and are given as:

$$\alpha = \frac{D_p^2 \varepsilon^3}{150(1-\varepsilon)^2} \qquad C_2 = \frac{3.5(1-\varepsilon)}{D_p \varepsilon^3}$$

where D_p is the mean particle diameter of the packed bed and ε is the void fraction (defined as the void volume divided by the volume of the packed bed). The particle diameter (D_p) for the porous medium representing the TM is evaluated by the relation ($\frac{\varepsilon}{1-\varepsilon} D_p = d$), where d is the pore size. It is assumed here that the TM is a homogeneous porous matrix with an ordered arrangement of particles and interstitial pores.

Boundary Conditions

The iris and cornea are modeled as stationary rigid boundaries, and no-slip boundary condition is imposed along these surfaces. The normal secretion rate from ciliary body is 2.5 μl/min and to satisfy this inlet flow rate through the pupil, (circular aperture of radius 2.5 mm), a flat inlet flow profile of 2.12 μm/s magnitude is used for all simulations except for the cases where the pupil size is varied. Since most of the flow drains out into the aqueous veins passing radially through the TM, and the collector channels, the upper and lower surfaces of the annular TM are assumed to be impermeable walls (no-slip boundary condition). The pressure in the aqueous veins under normal condition is 9 mmHg,[14] so the outlet boundary is treated as a pressure outlet boundary condition with a specified pressure of 9 mmHg (1.2 kPa). The inclusion of the TM in the present simulation, and the incorporation of a realistic pressure outlet boundary condition, is a distinct improvement over previously reported efforts.[1,10–12]

For the temperature, the iris and the incoming flow through the pupil are specified to be at the core body temperature (37°C). The temperature of the cornea is set at constant value, which is varied from 31 to 36.98°C to understand the importance of buoyancy in AH dynamics. The large temperature difference studied (6°C) reflects the upper end of potential temperature gradients in the eye, and may be reflective of conditions in extremely cold climates. The lowest temperature difference studied (0.02°C) represents conditions when the eye-lids are closed, and the corneal surface is not directly exposed to the ambient. Under these conditions, buoyancy effects are likely to be relatively weaker, and the details of the inflow velocity profile through the pupil may play an increasingly important role. The choice of Dirichlet boundary condition on the corneal shell is based on the results of the previous experiments and simulations,[1,23,28] which predicts the corneal temperatures to be 37±0.5°C and a temperature difference of 2°C across the anterior chamber.

NUMERICAL PROCEDURE

The commercial CFD-package FLUENT is used for all simulations reported in the present work. The numerical procedure is based on a control volume approach where the computational domain is divided into a number of cells or elements, and the governing equations discretized into algebraic equations in each element. The control-volume approach leads to discretization equations, which express the integral conservation of mass, momentum, and energy in each control volume. The discrete values of the variables are stored at the cell-centers, but the convection terms in the discretized equation must be interpolated at the cell faces from the cell-center values. A second-order upwind scheme is used for deriving the face values of different variables in the momentum and energy equations. For the pressure equation, a second-order accurate discretization scheme is used. For preserving second-order accuracy, a multidimensional linear construction approach is used to compute the quantities at the cell interfaces. In this approach Taylor-series expansion of the cell-centered solution about the cell centroid is used, and the face value ϕ is computed using $\varphi_f = \varphi + \nabla\phi \cdot \Delta\vec{S}$ where ϕ is the cell-centered value in the upstream cell and $\Delta\vec{S}$ is the displacement vector from the upstream cell to the face centroid.

A structured multiblock solver is used for the numerical solution. The system of algebraic equations are solved using the Gauss–Siedel scheme. Although the Gauss–Siedel scheme rapidly removes the high frequency errors in the solution, low frequency errors are reduced at a rate inversely proportional to the grid size. A W-cycle multigrid scheme is used to accelerate the convergence by applying corrections on the coarser grid-levels. The coupling between velocity and pressure is handled using the SIMPLEC-algorithm,[2] which uses the conservation of mass equation to derive a pressure corrector equation, and uses a pressure and velocity correction step to yield continuity satisfying velocity fields at each iteration.

The equations in the porous region (TM) are solved simultaneously with the equations in the anterior chamber region. To avoid exacerbating convergence issues, it is

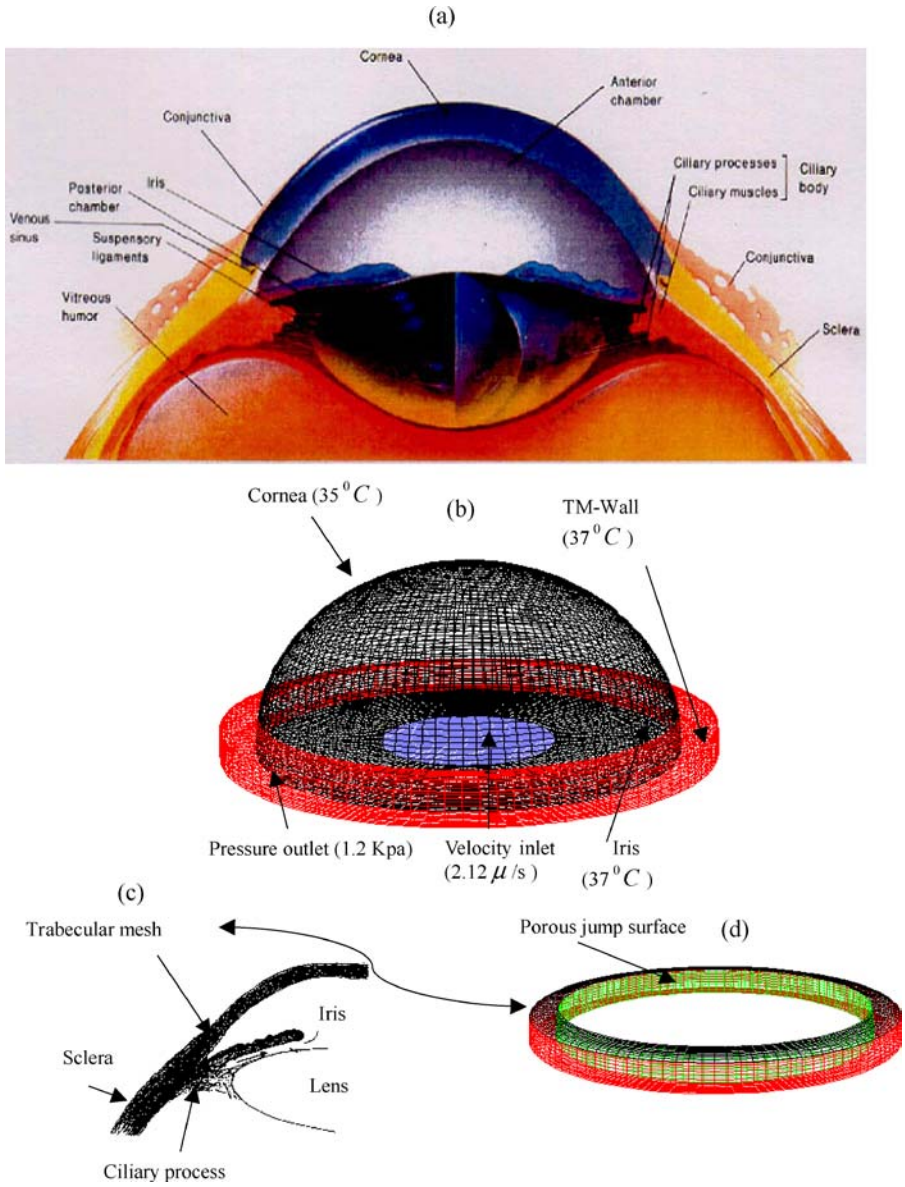

FIGURE 1. (a) Schematic of a Rabbit's eye, (from Mullenax[24]). (b) Geometrical model used for the simulation. (c) Details of the anterior chamber (from Huillier and Sbirlea[13]). (d) Model of TM.

critical to have high quality orthogonal grids with moderate aspect ratios. The commercial package GRIDPRO was used in the grid generation process and only hexahedral cells of aspect ratio less than three in the computational domain is used. The geometry is divided into 29 blocks, with four blocks representing the porous zone, five blocks located in the core of the hemispherical anterior chamber, and the remaining 20 blocks defining the periphery (Fig. 1). For the cases reported in this paper, 300,000 hexahedral cells are used. To demonstrate grid independence, simulations are run with 600,000 and 1,000,000 cells. Less than 2% variation in the magnitude of the maximum velocity is observed between the 300,000 cell calculation and the 1,000,000 cell calculation (Fig. 2(b)), and justifies the use of 300,000 cells for the simulations.

RESULTS AND DISCUSSION

Role of Buoyancy

In order to confirm the dominance of buoyancy as the driving mechanism for the AH dynamics, three simulations are performed for the horizontal upward-facing eye. These

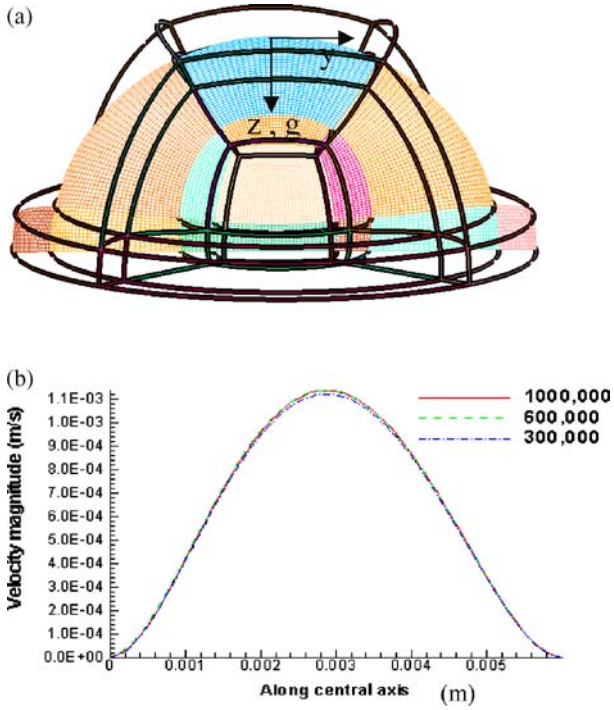

FIGURE 2. (a) Topology and mesh in the vertical mid-plane (center of the corneal-surface coincides with the zero of coordinate axis) (b) Velocity magnitude along the central axis of the anterior chamber for 300,000, 600,000, and 1,000,000 hexahedral cells (central axis starts from the corneal-center).

simulations are performed for a 2°C temperature difference between the iris and the corneal surface. The three simulations correspond to no-buoyancy (Fig. 3(a)), no inflow through the pupil (Fig. 3(b)), and combined inflow and buoyancy (Fig. 3(c)). For the no buoyancy case, the body force terms were not included in the momentum equations. For the no-inflow case, since a mass-conserving numerical procedure is employed, combined with pressure boundary conditions at the outlet, there is no outflow as seen in Fig. 3(b), and the AH simply recirculates in the anterior chamber due to buoyancy. Without buoyancy, the magnitude of the maximum velocity is 2.12 μm/s (which is the inlet velocity), while with buoyancy alone (Fig. 3(b)), the magnitude of the maximum velocity is 1020 μm/s, which is nearly 480 times greater than the no-buoyancy case. With combined buoyancy and inflow (Fig. 3(c)), the maximum velocity is nearly the same (within 10%) as with buoyancy alone (Fig. 3(b)) indicating that buoyancy is the dominant driving mechanism for the AH flow. The flow patterns are quite different with and without buoyancy, with a recirculating flow pattern and a corner vortex in the presence of buoyancy (Figs. 3(b) and 3(c)). Without buoyancy, the flow enters through the pupil and leaves through the TM without any recirculation or corner-vortex in front of the TM (Fig. 3(a)).

Effect of Inlet Profile

For analyzing the effect of the inlet velocity profile, simulations are performed for both a flat velocity profile and a parabolic velocity profile (Fig. 4(a)) at the inlet aperture of the anterior chamber. In both cases, the average velocity and mass flow rate through the aperture is maintained constant. The line plots of the velocity magnitude along the vertical centerline (Fig. 4(b)) does not show any difference between the two inlet profiles since the flow is primarily driven by the buoyancy forces, and the inlet velocity profile does not play a major role in altering the anterior chamber flow distribution.

Effect of Eye Orientation

Velocity Contours

As seen in Fig. 3, gravity plays a major role in determining the flow pattern of AH inside the anterior chamber. In the horizontal upward-facing position, (Fig. 5(a)) the gravity direction is perpendicular to the iris surface, and the flow field is axis-symmetric. In the vertical orientation (Figs. 5(b) and 5(c)), gravity destroys the symmetry in the vertical (Y–Z) plane. For these two orientations, the flow profiles and recirculation zones are completely different.

For the horizontal position (Fig. 5(a)), the warmer fluid entering the pupil rises upward, and moves down the corneal surface leading to two large symmetric recirculation zones. The highest velocities (1.14 mm/s) occur midway along the vertical axis of symmetry. Just next to the TM there is a smaller recirculation zone, which shows the effect of the resistance of TM on the outflow. All features of the flow field are identical about the vertical axis of symmetry including the exit flow rates through the left and right TM.

For the vertical orientation of the eye (Fig. 5(b)), the warmer fluid rises upward along the iris surface and then turns downwards as it encounters the higher resistance in the upper TM regions. The flow then descends along the corneal surface toward the lower TM. A portion of the recirculating flow exits through the small pores of the TM. Further, no secondary eddy is observed in the vicinity of the TM as in the horizontal configuration. The highest velocities are located near the middle of the iris surface (0.79 mm/s) and just upstream of the mid-corneal surface (0.627 mm/s). The stagnation zones and regions of large curvature are of special interest because particles or cells in the AH can get trapped in these regions and lead to the development of blockages, which can increase the IOP (e.g., as in pigmentary glaucoma). Clearly, in the vertical orientation the iris and the corneal surface are subjected to higher velocities and therefore shear stresses than in the horizontal orientation.

For the vertical orientation, the streamlines plotted in the horizontal mid-plane passing through the center of the pupil reflect the flow path of the AH, (Fig. 5(c)), produced by pressure differences in the horizontal mid-plane. In the horizontal plane, at each x-location, the cross-sectional area in the vertical plane is different with the maximum area at the mid-plane and minimum area at the TM end. Therefore, there is pressure variation (although small) in the x-direction with higher pressures at the corners (lower cross-sectional area) and lower pressure at the mid-plane (higher cross-sectional area). This pressure difference drives the flow in the horizontal plane from the corners to the center in the x-direction. In the z-direction, the cross-sectional area of the vertical plane is a minimum at the outermost corneal-surface location (lowest value of z), and therefore pressure increases as one moves away from the iris leading to a flow from the corneal surface toward the iris. From the iris, there is inflow through the pupillary opening.

In order to clarify the difference of flow profiles in TM, the velocity contours and streamlines are plotted separately in the region of TM for both horizontal and vertical orientations of the eye (Fig. 6(a–e)). The magnitude of the outflow velocity is of the order of 1 μ/s (Fig. 6(e)), and is comparable in both orientations. There is no significant variation of the outflow through the TM even in the vertical orientation. This is illustrated in Fig. 6(e) where the velocity magnitudes in the upper TM and lower TM are nearly identical. Reason for this is that the outflow through the TM is primarily controlled by the pressure drop and the resistance in the TM and the small circumferential pressure variations in front of the TM do not play a significant role in the outflow. One key difference in the vertical and horizontal cases is the presence of the recirculation zone in front of the TM for the horizontal orientation. Because of this recirculation upstream of the TM-corneal surface corner, a significant fraction of the TM outflow is routed past the

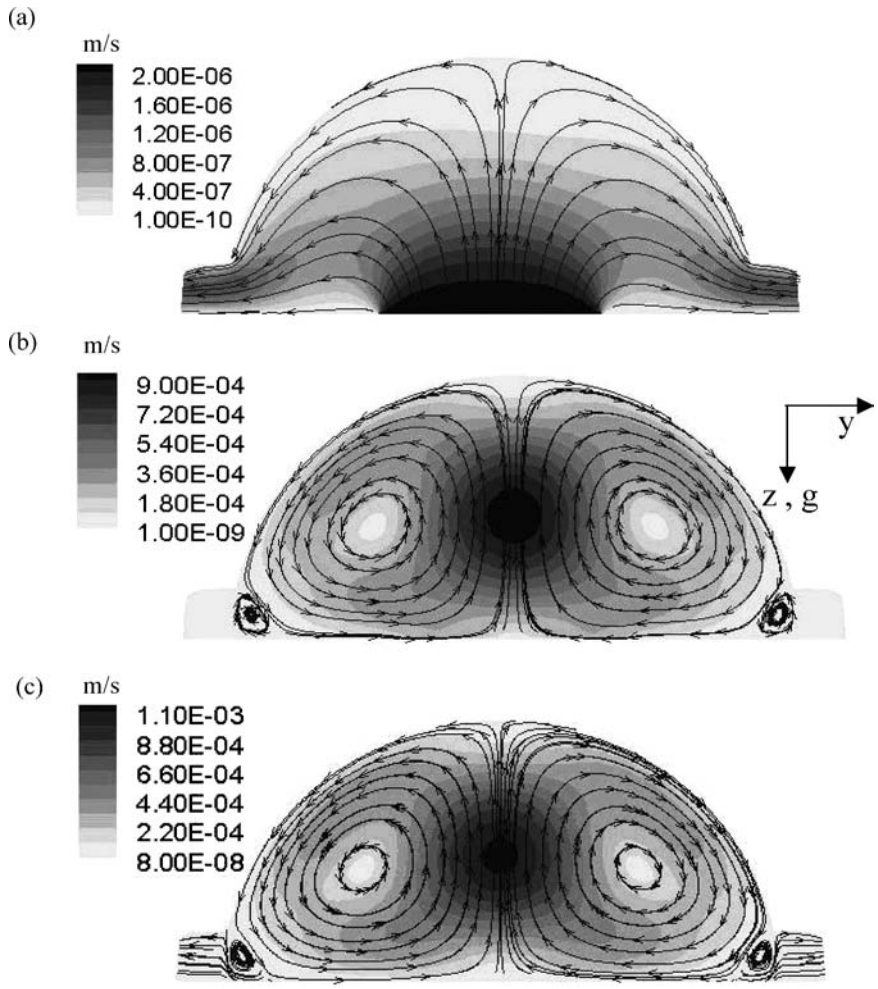

FIGURE 3. Streamlines and contours of velocity magnitude. (a) Without buoyancy, (b) with buoyancy and no inflow, and (c) with buoyancy and inflow. $\Delta T = 2°C$.

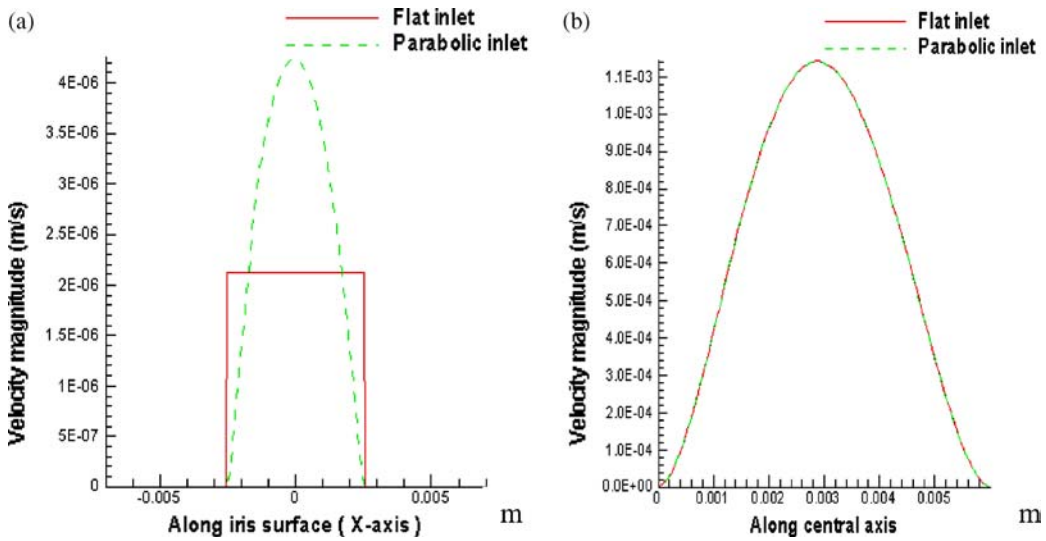

FIGURE 4. (a) Flat and parabolic velocity inlet profile. (b) Comparison of velocity magnitude along the central *Z*-axis for the flat and parabolic velocity inlet profile. $\Delta T = 2°C$, pore size = 0.6 μm, horizontal orientation.

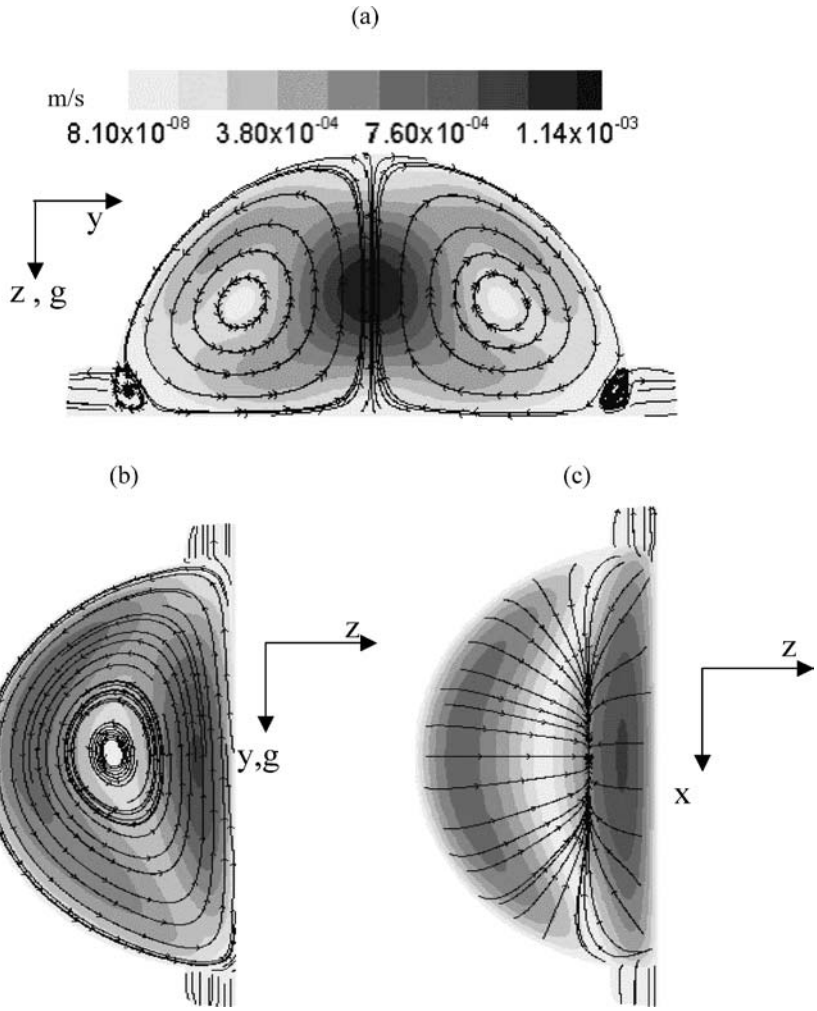

FIGURE 5. Streamlines and contours of velocity magnitude. (a) Horizontal orientation, vertical mid-plane; (b) vertical orientation, vertical mid-plane; and (c) vertical orientation, horizontal–mid-plane. $\Delta T = 2°C$, pore size = 0.6 μm.

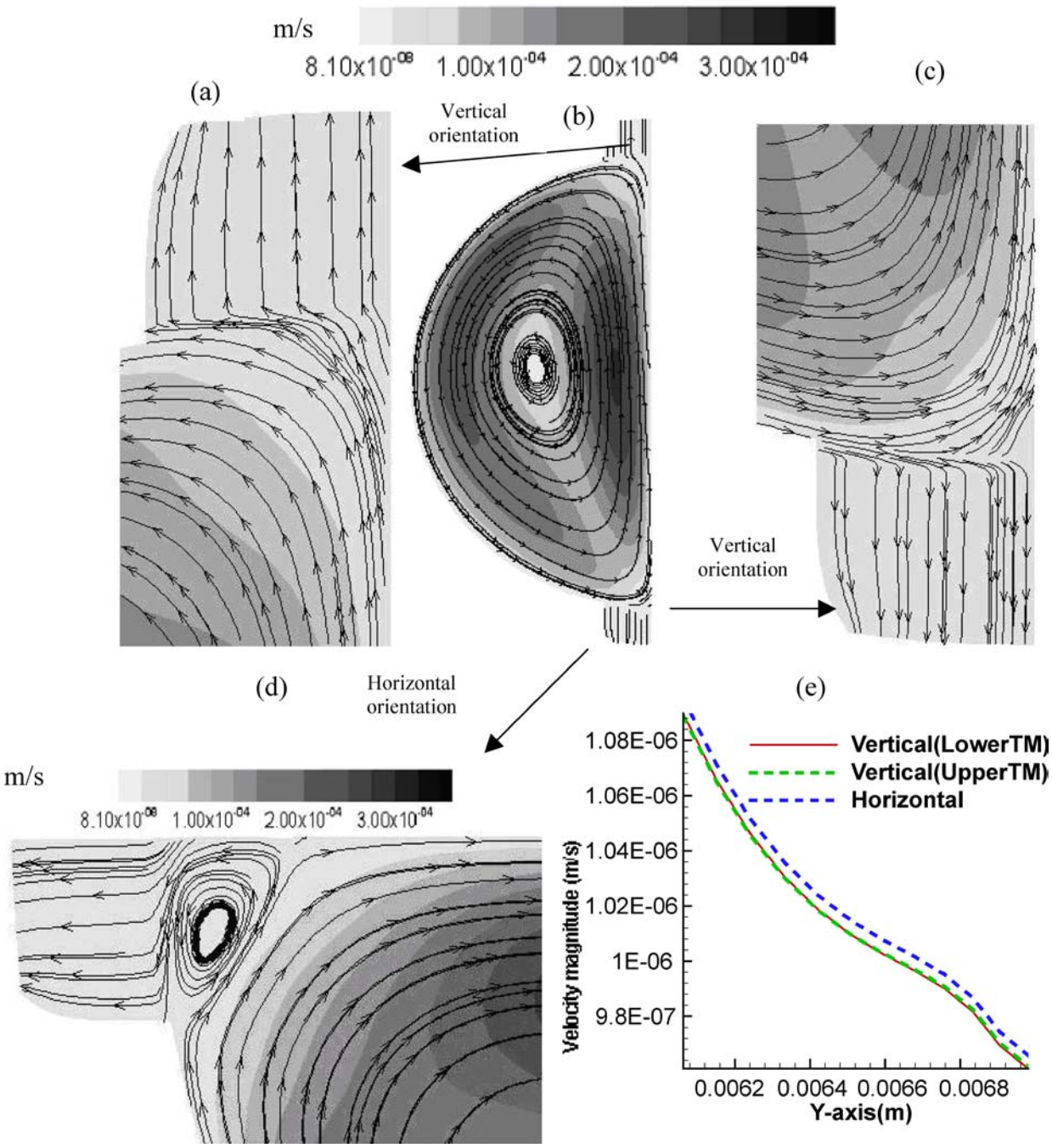

FIGURE 6. Streamlines and contours of velocity magnitude in TM, (a) upper part of TM, vertical orientation, vertical mid-plane; (b) cross-section of anterior chamber, vertical orientation, vertical mid-plane; (c) lower part of TM, vertical orientation, vertical mid-plane; (d) extended view of TM, horizontal orientation, vertical midplane; and (e) plot of velocity magnitude along centerline of TM in vertical midplane in the TM. $\Delta T = 2°C$, pore size = 0.6 μm.

TM-iris root junction in the horizontal orientation. This indicates the potential of protein or other particles being entrapped in the recirculation region leading to deposition in the TM and increased resistance to the outflow.

Temperature Contours

Contour plots for the temperature are shown in Fig. 7 for both the horizontal and vertical orientations of the eye. The AH gets heated as it moves toward the center

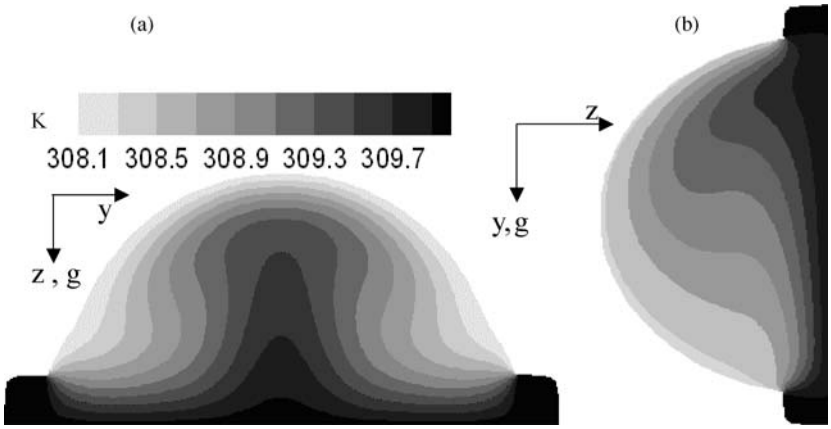

FIGURE 7. Contours of temperature. (a) Horizontal orientation, vertical mid-plane; and (b) vertical orientation, vertical mid-plane. $\Delta T = 2°C$, pore size = 0.6 μm.

of the pupil along the warmer iris surface. Consequently, the temperature gradient decreases from the iris root to the pupil center. The AH is warmest at the center, and due to buoyancy lifts up toward the cornea with a plume-like characteristic. Thus, buoyancy is responsible for generating the flow, and the plume-type thermal characteristic. The largest temperature gradients are located at the stagnation point (mid-point of the corneal surface) and these temperature gradients diminish rapidly as the flow descends along the relatively cooler corneal surface. For the vertical configuration, the temperature gradient is relatively high close to the lower root of the iris, which diminishes as flow rises vertically upwards along the heated iris surface. Along the corneal surface the highest temperature gradient occurs close to the upper regions as the flow turns along the cooler corneal surface due to resistance of the upper part of the TM. The flow gets cooled while descending along the corneal surface and temperature gradient attains its lowest value on the corneal surface near the lower part of the TM.

Pressure Contours

The pressure variations in the anterior chamber region are considerably smaller than the pressure drop across the porous TM and therefore the pressure contours in these regions are plotted separately in order to preserve clarity in the contour plots. Heys *et al.*[12] report in their simulations on the eye model that the pressure is essentially uniform inside the anterior chamber, which is supported by the present predictions. The pressure contours in the TM region are plotted in Fig. 8(a) for the horizontal eye orientation. Along the TM, from the anterior chamber to aqueous veins, the pressure decreases from the normal IOP of 15 mmHg (~1.93 KPa)[7] inside the anterior chamber to 9 mmHg (~1.2 KPa)[7] corresponding to the pressure in the veins. The pressure variations in the TM are relatively linear along the radial direction in the horizontal planes parallel to the iris surface, and appear to be nearly uniform normal to the iris surface, Figs. 8(a) and 8(b). Therefore, flow in the TM regions is essentially radially outwards from the anterior chamber to aqueous veins. It should be noted that in the present work the focus is on reproducing the correct pressure drop and the outflow velocity in the TM, and not in reproducing the details of the local pressure distributions in the TM. The modeling of the TM in the present case is representative of the entire outflow network, and comparison of local pressure distributions with experimental observations was not considered in view of lack of consensus of the data and the mechanisms leading to increased resistance in the TM pathway.

The pressure contours in the anterior chamber (excluding the TM-zone) are plotted in Figs. 8(c) and 8(d) for two different orientations of the eye. As mentioned earlier, the differences in pressure in the anterior chamber are very small and are related to velocity differences induced by the buoyancy driven flow. For the horizontal position, Fig. 8(c), the pressure is high close to the TM. The pressure is also high near the mid-point of the cornea, where the AH-velocity reduces as it approaches the stagnation point on the corneal surface. The pressure decreases from the stagnation point as the flow moves downward along the corneal surface until it reaches the iris–TM juncture where the pressure increases. In the vertical orientation (Fig. 8(d)), as the flow moves upwards along the iris surface, pressure decreases slightly. However, the added frictional resistance of the TM and the reduced cross-sectional area (with higher frictional drop) causes lower velocity and elevated pressure in the region close to the upper iris–TM juncture. As the AH descends along the corneal surface, the pressure decreases. However, beyond the corneal mid-point, the pressure begins to increase as the flow approaches the lower portion of TM. In the lower half of the anterior chamber higher pressures and lower velocities are encountered relative to the upper half. Thus, the lower half is likely to be more susceptible to particle deposition, build-up, and blockages. The pressure is relatively uniform across the horizontal plane in the vertical orientation.

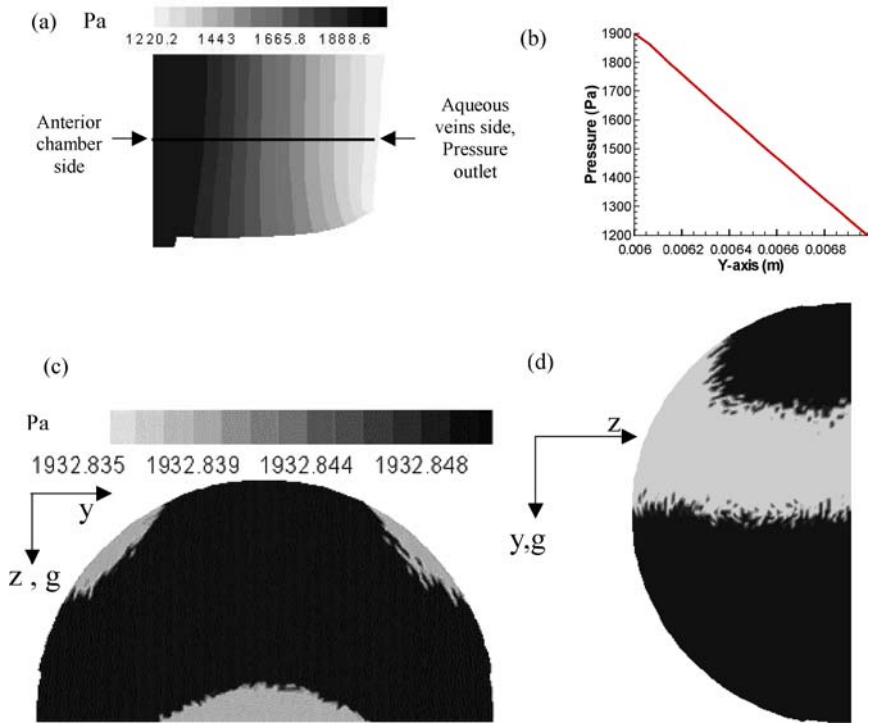

FIGURE 8. (a) Pressure-contours in the TM; (b) pressure magnitude along centerline of TM (along the line shown in Fig. 8a; (c) pressure-contours in horizontal orientation, vertical mid-plane; and (d) pressure-contours in vertical orientation, vertical mid-plane. $\Delta T = 2°C$, pore size = 0.6 μm.

Shear Stress Contours

The rubbing between the peripheral iris and anterior zonular packets causes most of the pigmentary liberation from the posterior iris surface in Pigment Dispersion Syndrome and Pigmentary glaucoma.[19] The anterior border layer of the iris is composed of fibroblasts and pigmented melanocytes, both of which are oriented parallel to the iris surface[29] and which could be the secondary source of pigment particles in the anterior chamber. The wall shear stress along the iris surface is analyzed to understand the role of shear stress in detaching the pigment granules from the anterior layer of the iris surface. For the two orientations of the eye the wall-shear stress is plotted in Fig. 9 for a $\Delta T = 2°C$. Tables 2 and 3 show the dependence of the average shear stress with ΔT which shows increasing shear stress with increasing temperature difference across the cornea. Canning *et al.*[1] derived a linear relationship between the wall shear stress at the iris surface and the temperature difference across the anterior chamber. This was given as $\tau_0 \sim 6.7 \times 10^{-4} \times \Delta T$ Pa for the vertical orientation of the eye. The wall shear stress in the present model also

TABLE 2. Nondimensional velocity, average Nusselt number, and Iris shear stress variation with temperature difference (Horizontal position).

	0.02°C	2°C	4°C	6°C
U_{max}/U_{inlet}	2.12	538	1024	1387
Nu (Nusselt Number)	4.54	5.56	6.18	6.56
Wall shear stress (Iris, Pa)	7.0×10^{-6}	1.16×10^{-3}	2.12×10^{-3}	2.94×10^{-3}

TABLE 3. Non-dimensional velocity, Average Nusselt No and iris shear stress variation with temperature difference (vertical position).

	0.02°C	2°C	4°C	6°C
U_{max}/U_{inlet}	6.7	373	552	680
Nu (Nusselt number)	4.54	5.49	6.12	6.56
Wall shear stress (iris, Pa)	2.0×10^{-5}	2.17×10^{-3}	3.79×10^{-3}	5.17×10^{-3}

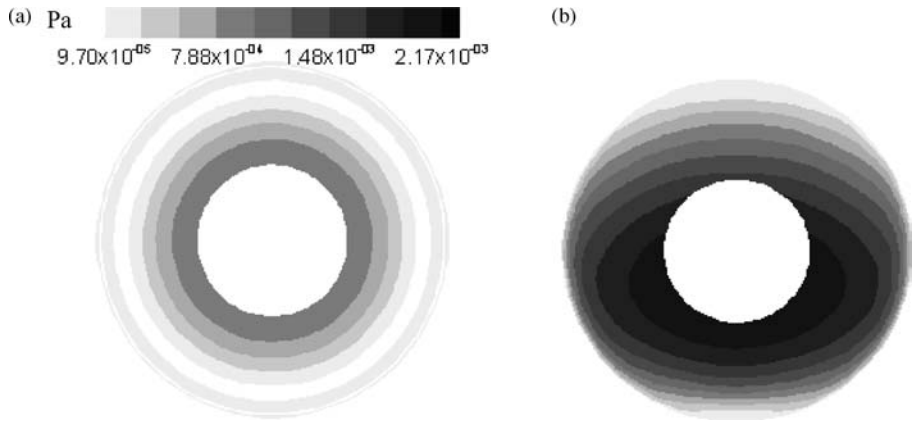

FIGURE 9. Wall shear stress plot for the anterior iris surface. (a) Horizontal orientation and (b) vertical orientation. $\Delta T = 2°C$, pore size = 0.6 μm.

shows an approximately linear relationship with ΔT, but the proportionality constant is 1.0×10^{-3}, which is 1.49 times larger then the constant predicted by Canning *et al*. This difference may be due to the simplifications applied in the model by Canning *et al*. in the momentum and energy equation, which allowed them to solve the equations in a closed form and avoid numerical simulations. The magnitude of the shear stress predicted is much less than that required for the endothelial cell detachment, which is in the range between 0.51 and 1.53 kg/m/s^2 as reported by Gerlach *et al*.[8] So it is unlikely that fluid shear stress could detach pigments from the anterior iris surface, but the plot of shear stress gives insight about the location on the iris surface from where the probability of detachment of the cells is maximum in case of some specific diseases or presence of free pigment granules in the anterior iris layer. For the horizontal orientation, the wall-shear stress is maximum near the inner periphery of the iris, while for the vertical position the maximum shear stress zone is located in the lower half of the iris surface close to the pupil (Figs. 9(a) and 9(b)).

Effect of ΔT Across the Anterior Chamber

As noted earlier, the driving mechanism for the AH is the temperature difference across the anterior chamber. A reasonable temperature difference between corneal and iris surface is $\Delta T = 2°C$, but conditions such as the outside ambient temperature, and whether the eye is open or closed, can cause variations in the corneal temperature. In this study, the temperature difference across the anterior chamber has been varied from 0.02 to 6°C, with 0.02°C corresponding to the case when the eye-lid is closed and the corneal temperature is close to the body temperature (Fig. 10(a)). The flow patterns and the velocity magnitudes are quite different between the 0.02°C and the 2°C cases. In the horizontal orientation of the eye, for the 0.02°C case, the center of the primary recirculation is shifted toward the iris surface and the magnitude of the maximum velocity is close to the inlet velocity through the pupil. Since the flow velocities are small the secondary re-circulation zone near the TM is not present any more. When the temperature difference is increased to 4°C (Fig. 10(c)), the profile is similar to the normal temperature difference (2°C) case but the magnitude of the maximum velocity is increased by a factor of 2. A similar profile is observed even for a temperature difference of 6°C with 2.57 times larger magnitude of maximum velocity compared to the 2°C temperature difference case.

For the vertical orientation of the eye, at a low ΔT of 0.02°C, the streamlines are skewed inwards close to the iris surface (Fig. 10(d)). This is because at this low ΔT, the buoyancy-induced flow is weak and comparable in magnitude to the inflow that enters the anterior chamber orthogonal to the iris surface. As a consequence, the resulting velocity vector near the pupil aperture is at an angle to the iris surface. When ΔT is increased to 2 or 4°C (Figs. 10(e) and 10(f)), the buoyancy induced flow directed upwards along the iris is considerably stronger (by an order of magnitude) than the inflow, and consequently the flow near the iris surface is essentially parallel to it. By increasing the temperature difference from 2 to 4°C, the increase in magnitude of the maximum velocity is 1.5 times, which is less than the two times increase for the horizontal orientation. Heys and Barocas[11] found that the velocity increased by 1.5 times when the temperature difference across the anterior chamber increased from 3 to 7°C, but the flow pattern itself was not significantly affected by this temperature increase. Thus, their observations are generally consistent with our predictions.

The average heat flux across the cornea for $\Delta T = 2°C$ is 550 W/m^2 and for $\Delta T = 4°C$ is 1230 W/m^2, which is in agreement with the results of Heys and Barocas,[11] who

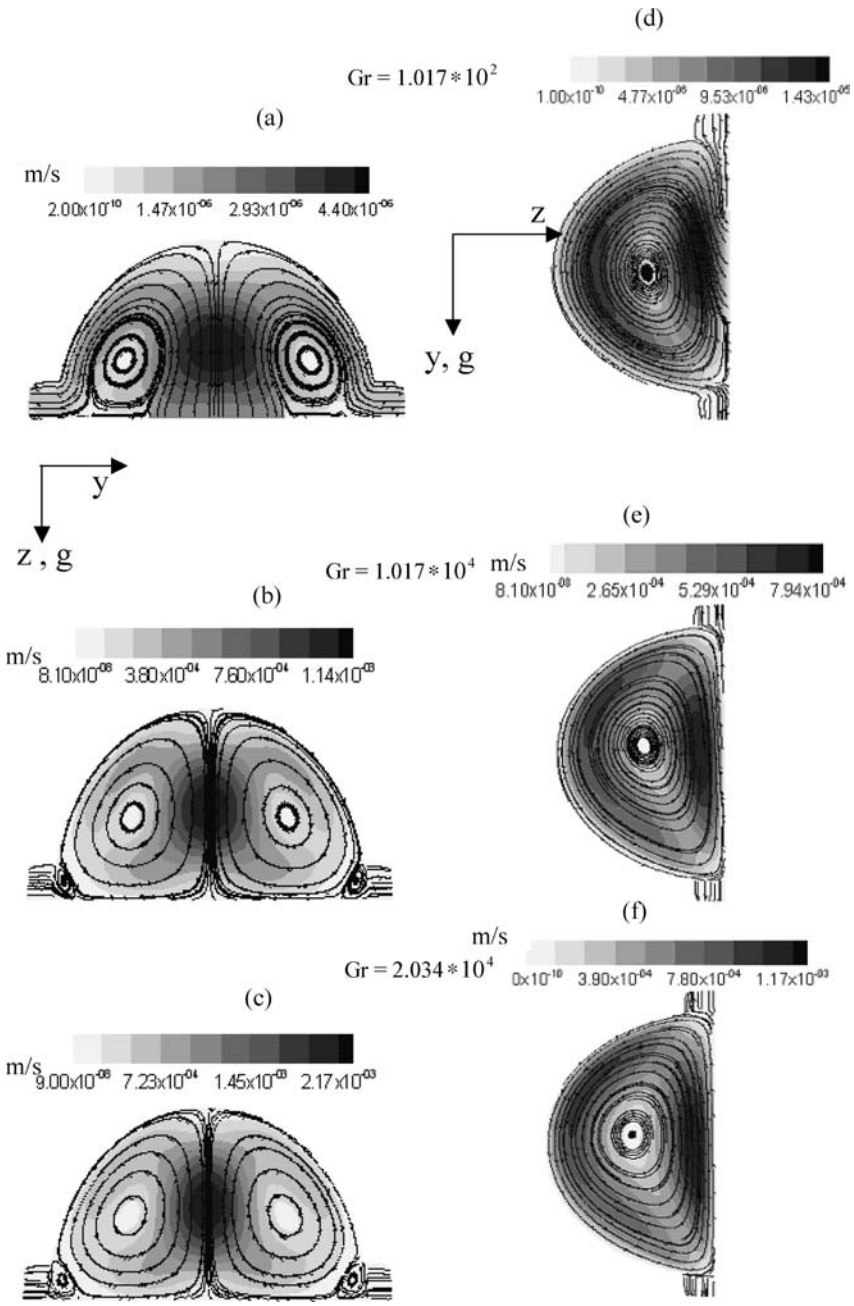

FIGURE 10. Velocity–magnitude contour plot in vertical mid-plane. Horizontal orientation, (a) $\Delta T = 0.02°C$, (b) $\Delta T = 2°C$, and (c) $\Delta T = 4°C$. Vertical orientation, (d) $\Delta T = 0.02°C$, (e) $\Delta T = 2°C$, and (f) $\Delta T = 4°C$.

report the average heat flux of 800 W/m^2 for $\Delta T = 3°$C. For the horizontal and vertical orientation respectively, Tables 2 and 3 report the nondimensional maximum velocity, the average Nusselt number and the shear stress for different values of ΔT across the anterior chamber. There is a difference of two orders of magnitude in maximum velocity inside the anterior chamber when ΔT is increased from 0.02 to 6°C, which shows the dominance of buoyancy on AH flow inside the eye. The non-dimensional heat transfer coefficient (Nusselt number, Nu) at the corneal surface shows increases with increasing temperature differences. For both orientations of the eye, Nu has the same value (4.56) at $\Delta T = 0.02°$C (expected since buoyancy does not play a major role) and increases to 6.56 for $\Delta T = 6°$C. The similar values for Nu for the two orientations at ΔT of 6°C is somewhat unexpected since buoyancy is important at this ΔT, and the flow patterns are different. However, these are average values and while the averages are close, significant differences in the local values are obtained. As noted earlier, the wall shear stress on the iris surface has

approximately linear relationship with ΔT. The constant of proportionality for horizontal orientation of the eye is 0.53 $\times 10^{-3}$ while for the vertical orientation it is 1.0×10^{-3}. Clearly the shear stress values are significantly influenced by the orientation of the eye, with values for the vertical orientation that are nearly two times those of the horizontal orientation.

Effect of Pupil Size

Since the size of the pupil opening varies with the intensity of the light in the surroundings, we simulated the flow for two different diameters of the pupil—5 mm and 3 mm. The same flow rate and depth of the anterior chamber was maintained. No major change in the IOP or velocity profile of the AH is observed. This behavior of the flow is a consequence of almost negligible effect of inlet velocity on the flow profile and the dominance of buoyancy.

CONCLUDING REMARKS

A three-dimensional model for the anterior chamber of the eye is developed in order to investigate the flow and pressure distribution inside the eye. The computational model includes a two-layer porous matrix model for the complex Trabecular Meshwork. The IOP predicted inside the anterior chamber and the pressure drop across the TM (corresponding to real pore size of the JCT) are found to be close to experimental observations for a normal eye. The following major observations are made from the computed results.

1. Predictions verify the dominance of the buoyancy as the driving mechanism for the AH flow.
2. The two orientations of the eye, horizontal and vertical, lead to different flow patterns and temperature distributions. The horizontal orientation leads to corner recirculation along the iris–TM junction while no such corner recirculation is observed for the vertical orientation.
3. The pressure drop mostly occurs across the TM. Within the anterior chamber, the variations in pressure are relatively small.
4. The surface shear is higher in the vertical orientation (by a factor of nearly 2). The surface shear is correlated with pigmentary cell removal, but the levels in the anterior chamber are not high enough to lead to cell removal. The average Nusselt number is not significantly influenced by the orientation of the eye, although there are significant differences in the local values.
5. The temperature gradient across the anterior chamber is the key parameter controlling velocity magnitudes, and shear rates. Increasing the temperature difference from 0.02°C to 6°C produces increases in the velocity magnitudes by greater than two orders of magnitudes and comparable increases in shear stress. The average shear stress is shown to have a linear dependence on the temperature difference.
6. The pupil opening has little or no influence on the AH flow pattern or velocity magnitudes.

ACKNOWLEDGMENTS

This work was supported by a grant from the Louisiana Board of Regents under a Health Excellence Support Fund program. Their support is gratefully acknowledged.

REFERENCES

[1]Canning, C. R., J. N. Dewynne, A. D. Fitt, and M. J. Greaney. Fluid flow in the anterior chamber of a human eye. *IMA J. Math. Appl. Med. Biol.* 19:31–60, 2002.

[2]Doormal, J. P., and G. D. Raithby. Enhancements of the SIMPLE method for predicting incompressible fluid flow. *Numer. Heat Transf.* 7:147–163, 1984.

[3]Epstein, D. L., T. F. Freddo, P. J. Anderson, M. M. Patterson, and S. B. Chu. Experimental obstruction to aqueous outflow by pigment particles in living monkeys. *Invest. Opthalmol. Vis. Sci.* 27:387–395, 1986.

[4]Ergun, S. Fluid flow through packed columns. *Chem. Eng. Prog.* 48(2):89–94, 1952.

[5]Ethier, C. R., M. F. Coloma, A. W. Kater, and R. R. Allingham, Retroperfusion studies of the aqueous outflow system. *Invest. Opthalmol. Vis. Sci.* 34:(2):385–394, 1992.

[6]Ethier, C. R., R. D. Kamm, M. Johnson, A. F. Pavoo, and P. J. Anderson, Further studies on the flow of aqueous humor through microporous filters. *Invest. Opthalmol. Vis. Sci.* 30:739–746, 1989.

[7]Ethier, C. R., R. D. Kamm, B. A. Palaszewski, M. C. Johnson, and T. M. Richardson. Calculations of flow resistance in the juxtacanalicular meshwork. *Invest. Opthalmol. Vis. Sci.* 27:1741–1750, 1986.

[8]Gerlach, J. C., G. Hentschel, K. Zeilinger, M. D. Smith, and P. Neuhas. Cell detachment during sinusoidal reperfusion after liver preservation, *in vitro* model. *Transplantation* 64:907–912, 1997.

[9]Grant, W. M., Experimental aqueous perfusion in enucleated human eyes. *Arch. Ophthalmol.* 69(6):783–801, 1963.

[10]Heys, J. J., and V. H. Barocas. Computaional evaluation of the role of accommodation in pigmentary glaucoma. *Invest. Opthalmol. Vis. Sci.* 43:700–708, 2002.

[11]Heys, J. J., and V. H. Barocas. A boussinesq model of natural convection in the human eye and the formation of Krukenberg's spindle. *Ann. Biomed. Eng.* 30:392–401, 2002.

[12]Heys, J. J., V. H. Barocas, and M. J. Taravella. Modeling passive mechanical interaction between aqueous humor and iris. *J. Biomech. Eng.* 123:540–546, 2001.

[13]Huillier, J. P., and G. A. Sbirlea, T. B. Martonen. Morphology of the human eye: Glaucoma physiology and laser iridectomy. In: Medical Applications of Computer Modelling: Cardiovascular and Ocular Systems, edited by WIT, United Kingdom, pp. 225–242, 2000.

[14]Johnson, M. C., and R. D. Kamm. The role of Schlemm's canal in aqueous outflow from the human eye. *Invest. Opthalmol. Vis. Sci.* 24:320–325, 1983.

[15]Johnson, M. C., R. D. Kamm, W. M. Grant, D. L. Epstein, and D. Gasterland. The flow of aqueous humor through micro-porous filters. *Invest. Opthalmol. Vis. Sci.* 27:92–97, 1986.

[16]M. Johnson, A. Shaprio, C. R. Ethier, and R. D. Kamm. Modulation of outflow resistance by the pores of the inner wall endothelium. *Invest. Opthalmol. Vis. Sci.* 33:1670–1675, 1992.

[17]Kocak, I., S. Orgul, and J. Flammer. Variability in the measurement of corneal temperature using a non-contact infrared thermometer. *Ophthalmologica* 213(6):345–349, 1999.

[18]Lindenmayer, J. M., M. G. Kahn, E. Hertzman, and D. L. Epstein. Morphology and function of the aqueous outflow system in monkey eyes perfused with sulfhydryl agents. *Invest. Opthalmol. Vis. Sci.* 24:710, 1983.

[19]Lehto, I., P. Ruusuvaara, and K. Setala. Corneal endothelim in pigmentary glaucoma and pigment dispersion syndrome. *Ophthalmologica* 68:703–709, 1990.

[20]Mallinson, G. D., and G. D. V. Davis. Three-dimensional natural convection in a box: A numerical study. *J. Fluid Mech.* 83(1):1–31, 1977.

[21]McEwen, W., Application of Poiseuilles's law to aqueous outflow. *Arch. Ophthalmol.* 60(2):290–294, 1958.

[22]Mclaren, J. W., S. D. Trocme, S. Relf, and R. F. Brubaker. Rate of flow of aqueous humor determined from measurements of aqueous flare. *Invest. Opthalmol. Vis. Sci.* 31(2):339–346, 1990.

[23]Mori, A., Y. Oguchi, Y. Okusawa, M. Ono, H. Fyhusguna, and K. Tsubota. Fujishima, and use of high-speed, high-resolution thermography to evaluate the tear film layer. *Am. J. Ophthalmol.* 124:729–735, 1997.

[24]Mullenax, C. A., "Doctoral Research Prospectus," available at (http://www.studentweb.Tulane.edu/∼cmullen/documents.html), pp. 6.

[25]Okuno, T. Thermal effect of infra-red radiation on the eye: A study based on a model. *Ann. Ocuup. Hyg.* 35:1–12, 1991.

[26]Palkama, A., and R. Beureman. Ocular fluid dynamics measured with *vivo* confocal microscopy and microbeads. *Ophthalmology*, 2001.

[27]Scott, J. A. The computation of temperature rises in the human eye induced by infrared radiation. *Phys. Med. Biol.* 33:243–257, 1988.

[28]Scott, J. A., A finite element model of heat transport in the human eye. *Phys. Med. Biol.* 33:227–241, 1988.

[29]Tripathi, R. C., and B. J. Tripathi. Anatomy of the Human Eye, Orbit, and Adnexa. In: The Eye, Vol. 1a, Vegetative Physiology and Biochemistry, edited by Hugh Davson. New York: Academic, pp. 1–268, 1984.

[30]Yedder, R. B., and E. Bilgen. Laminar natural convection in inclined enclosures bounded by a solid wall. *Heat Mass Transf.* 32:455–462, 1997.